

1
2 **Diurnal Variation of Tropical Ice Cloud Microphysics:**
3 **Evidence from Global Precipitation Measurement Microwave Imager**
4 **(GPM-GMI) Polarimetric Measurements**
5

6 Jie Gong¹, Xiping Zeng², Dong L. Wu³, Xiaowen Li⁴
7

8 1. GESTAR Program, Universities Space Research Association, Columbia, MD

9 2. U.S. Army Research Laboratory, Adelphi, MD

10 3. NASA Goddard Space Flight Center, Greenbelt, MD

11 4. GESTAR Program, Morgan State University, Baltimore, MD
12

13 Corresponding author: Jie Gong (Jie.Gong@nasa.gov)
14

15 **Key points:**
16

17 1. The first study of the diurnal cycle of tropical ice cloud microphysics using spaceborne high-
18 frequency microwave polarimetric measurements.

19 2. The polarimetric difference's (PD's) diurnal cycle precedes that of the ice cloud occurring
20 frequency and total mass by about 2 hours.

21 3. The diurnal cycle of PD can be explained by changes of the ice crystal axial ratio using
22 radiative transfer calculations.
23

Abstract

The diurnal variation of tropical ice clouds has been well observed and examined in terms of the occurring frequency and total mass but rarely from the viewpoint of ice microphysical parameters. It accounts for a large portion of uncertainties in evaluating ice clouds' role on global radiation and hydrological budgets. Owing to the advantage of precession orbit design and paired polarized observations at a high-frequency microwave band that is particularly sensitive to ice particle microphysical properties, three years of polarimetric difference (PD) measurements using the 166 GHz channel of Global Precipitation Measurement Microwave Imager (GPM-GMI) are compiled to reveal a strong diurnal cycle over tropical land (30°S–30°N) with peak amplitude varying up to 38%. Since the PD signal is dominantly determined by ice crystal size, shape, and orientation, the diurnal cycle observed by GMI can be used to infer changes in ice crystal properties. Moreover, PD change is found to lead the diurnal changes of ice cloud occurring frequency and total ice mass by about 2 hours, which strongly implies that understanding ice microphysics is critical to predict, infer, and model ice cloud evolution and precipitation processes.

Plain Language Summary:

Along with the rising and setting of the Sun, our Earth's clouds vary between day and night. For tropical ice clouds, there are many evidences showing that the cloud cover and thickness change dramatically during a day (referred to as the "diurnal cycle") but few hints of what happens to individual ice crystals. Using a new spaceborne satellite instrument called GPM-GMI, we found that ice crystal size or shape also exhibits a strong diurnal cycle over tropical land but not over

tropical ocean. We can further infer that the microscopic variation of ice crystals may be an important reason for the change of ice cloud cover and thickness later on.

1. Introduction

Upper tropospheric ice clouds, namely anvils and cirrus, spread to cover vast areas and persist for hours to days. They are a major modulator of Earth's radiation and thus play an important role in weather and climate changes (e.g., Hartmann et al., 1984; Raymond and Zeng, 2000; Waliser et al., 2009). Studies have shown that the cloud radiative effect (CRE) of the clouds strongly depends on physical details, such as cloud top height (Kiehl, 1994), thickness (Hong et al., 2016; Hartmann and Berry, 2017), overlaying situation (Hartmann et al., 2001), and microphysical properties (Liou et al., 2002; Zeng et al., 2009a, b; Tang et al., 2017). Fu and Liou (1993), for example, showed that the radiative heating rate for a layer of ice cloud with a fixed ice water path could differ by a factor of 10 when the mean effective radius of the ice particles varies by a factor of 5. Reducing the uncertainty of CRE requires a better understanding of ice cloud microphysical properties, which is essential not only to remote sensing of the bulk optical properties but also to the simulation of CRE (Tang et al., 2017). In addition, ice clouds, especially the anvils and mixed-phase clouds in deep convections, contribute much to tropical precipitation and vertical circulations (e.g., Raymond and Zeng, 2000; Liu and Zipser, 2008). Since ice clouds play a critical role in the global water and energy cycles, it is imperative to determine their microphysical processes as well as their macro-characteristics.

One of the large variabilities of tropical ice clouds is their strong response to the diurnal variation of solar heating at the Earth's surface (Yang and Slingo, 2001; Tian et al., 2004; Hong et al., 2006). The diurnal variations of ice clouds have been observed using various cloud

properties such as occurring frequency, total mass, and cloud cover with a variety of measuring techniques (e.g., Tian et al., 2004; Liu and Zipser, 2008; Eriksson et al., 2010; Millan et al., 2013; Jiang et al., 2014) in conjunction with some other key atmospheric variables such as water vapor (Soden, 2000), surface temperature (Dai et al., 2004) and convective activity (Chung et al., 2007). These metrics have been extensively studied over the past two decades especially owing to the rapid advance in spaceborne instrument technology, as well as the increase in a satellite's spatial and temporal coverage. However, microphysical properties of ice crystals, such as crystal shape, orientation, and size distribution, have rarely been investigated, since it is a challenge to observe ice crystal microphysical properties accurately from space. Some of the integrated properties (e.g., effective diameter) are derived products from primary properties, such as mass, coverage, and type, in most satellite observations (e.g., CloudSat) with arbitrary assumptions. Although new retrieval techniques such as one-dimensional variation method (1DVAR) and neural network can retrieve all desired variables together at least theoretically, oversimplified microphysical assumptions are still required in the retrieval model or training database, which directly impact their outputs (e.g., Boukabara et al., 2011; Duncan and Kummerow, 2016). Hence, how to observe and analyze the diurnal variation of cloud ice microphysics from space is inherently a difficult yet interesting topic.

Polarimetric difference (PD) between paired vertically and horizontally polarized (V-pol and H-pol hereafter for abbreviation) channels at a fixed incidence angle is a relatively matured product and can be measured precisely from space. Recently, the polarimetric data have been used to study ice microphysical properties (e.g., Skofronick-Jackson et al. 2015; Homeyer and Kumjian, 2015; Hioki et al., 2016). In particular, studies of PD from passive and active spaceborne measurements at visible and microwave wavelengths show that nonspherical ice

crystals are not randomly oriented but usually horizontally oriented (Prigent et al., 2001, 2005; Davis et al., 2005, 2007; Zhou et al., 2012; Defer et al., 2014). Gong and Wu (2017) (GW17 hereafter) first identified the similar features from the GPM-GMI 166 and 89 GHz observations. Taking advantage of GPM's precession orbit, this paper aims to better understand the diurnal variation of PDs in the tropics and its implication for ice crystal's microphysical properties and how they vary together with macroscopic quantities such as cloud occurring frequency and mass.

2. Diurnal Variations of 166 GHz Polarimetric Radiance Difference

The GPM core satellite has a dual-frequency precipitation radar (DPR) and a passive GMI instrument with 13 channels between 10 and 190 GHz (Hou et al. 2014; Skofronick-Jackson et al. 2015). Among the 13 channels, the 10.65, 18.7, 36.5, 89, and 166 GHz channels have V-pol and H-pol. In this study, only the 166 GHz polarization data are used because this channel is sensitive to cloud ice scattering and its PD is not sensitive to water cloud emission. Furthermore, the PD at this channel is least contaminated by surface polarizations in the tropics (GW17). The GPM core satellite flies at the altitude of 407 km in a non-Sun-synchronized orbit that covers a latitude range between 68°S and 68°N. It slowly progresses over the local solar time (LST), making it ideal to study the diurnal variability of clouds and precipitation. The GMI has a forward conical scan viewing geometry off-nadir at an angle of 48.5° (see Skofronick-Jackson et al. 2015 for details).

The current study uses Version 1.4 of Level-1C inter-calibrated GMI brightness temperature (TB) observations at 166 GHz during February 2014 – December 2016 (GPM X-Cal Working Group, 2015). The diurnal cycle is not separated further by seasons, as the seasonality in the tropics between 30°S and 30°N is small. Furthermore, since it takes approximately 45 days for

the GPM satellite to preprocess through all LSTs, integration over three years on a time interval of 2 hours can generate robust and useful cloud statistics. The GMI 183 ± 3 GHz radiance is used to screen the “confident cloudy-sky” scenes for estimating the cloud occurring frequency (OF) and the mean cloudy-sky TB (TB_{cld}). The colder TB_{cld} is, the thicker the ice cloud is. As at 166 GHz, $-TB_{\text{cld}}$ is roughly linearly correlated with the column-integrated ice water path (IWP) as long as the cloud is not completely opaque (Gong and Wu, 2014). Therefore, $-TB_{\text{cld}}$ can be used as a proxy for IWP along the GMI’s line of sight. Both 166 and 183 ± 3 GHz channels belong to the high-frequency group that scans simultaneously with the same footprint size of $4.2 \times 7.0 \text{ km}^2$. The “ 3σ cloud detection” threshold is employed to distinguish between clear- and cloudy-sky scenes, which is identical to Gong and Wu [2014; 2017]. This method first identifies the peak (TB_{peak}) and standard deviation (σ) of the probability density function (PDF) of the TB observations in a given region or a latitude belt over the period of interest, and then the cloudy-sky scene is defined at places where $TB < TB_{\text{peak}} - 3\sigma$. In practice, this procedure is iterated twice to remove the broadening effect introduced by clouds (i.e., bias in σ). Since a large amount of “possible ice cloud present” scenes with relatively warmer TB is excluded using this method, OF is much smaller and TB_{cld} is cold-biased. However, to fully describe the ice cloud polarization feature, it is necessary to account for the polarization signal corresponding to these “warmer ice cloud” scenes that are in general populated with cirrus and thin anvil clouds. Hence, another threshold is proposed in the next paragraph to separate the clear-sky and cloudy-sky polarimetric signatures.

Three years of the 166 GHz observations in the tropics (30°S - 30°N) are sorted to the nearest LST slot that is separated by a 2-hour interval. Then, the 2D PDF integration is performed for each of the 12 LSTs according to its V-pol TB (TB_V) and PD values. PD is defined as

$$PD \equiv TB_V - TB_H \quad (\text{Eqn 1})$$

A positive PD implies that the upwelling microwave radiation must have a shorter cloud optical length in V-pol (τ_V) than in H-pol (τ_H) due to either scattering or absorption along the path and vice versa. Once the PDF is compiled, the mean and standard deviation of the PD value within each TB_V bin is then calculated to draw the final curves shown in Fig. 1a for the oceanic and Fig. 1b for the landmasses, respectively. The cloudy-sky thresholds are drawn in the black dash lines. Following GW17, the bottom-up bell curve is referred to as the “PD-TB” relationship. The same as found in GW17, the TB_V value corresponded to the peak PD robustly located at approximately 200 K, and the broadness of the spread is strikingly similar across different LSTs. These features again reveal an apparently nearly universal bell-curve in the PD-TB relationship. These curves spread out at the peak PD but converge to roughly the same TB values as PD values approach zero. At the warm TB end when the curves converge, another threshold (dash-dot lines) is set, to the left of which is considered a full cloudy-sky PD-TB relationship. Since the dynamic range of TB_V for the PD-TB relationship holds the same during a day, the curvature of the curve is solely determined by its peak value of PD (PD_{peak}).

The PD_{peak} from tropical clouds exhibits a clear diurnal cycle over land but not over ocean. The amplitude of PD_{peak} variation over land is $\sim 38\%$ and that over ocean is only $\sim 6\%$. Furthermore, the maximum and minimum of PD_{peak} occur at local morning (9:00 LST) and afternoon (16:00 LST) over land, while the difference is not statistically significant over ocean. The general conclusion of local morning maximum and afternoon minimum of PD_{peak} over land is robust against using different time intervals (1 hr and 3 hrs), although the exact LST may vary by ± 1 hr. As will be shown in the next section, PD_{peak} , or the curvature of the curve, is the key variable to correspond to the column-integrated optical axial ratio.

The diurnal variation of PD_{peak} is better exhibited in Fig. 2a (ocean) and 2b (land) where PD_{peak} clearly shows an anticorrelation with cloud occurrence frequency and mean cloud TB. Compared to the diurnal cycle of upper-tropospheric clouds previously identified using Tropical Rainfall Measurement Mission (TRMM)'s precipitation radar and visible and infrared scanner, the diurnal cycle of PD_{peak} also anticorrelates with that of the area and cloud fraction for both ocean and land surface conditions. In those analyses, over ocean, the diurnal cycle of PD_{peak} precedes that of the precipitation rate (PR) by ~ 2 hrs, but for land cases, it lags the PR diurnal cycle by ~ 2 hrs (reference: Fig. 7 of Hong et al., 2006; Fig. 3 of Liu and Zipser, 2008).

To showcase the direct correlation of the diurnal cycles between PD_{peak} and the macro-quantities of the same group of clouds, Fig. 2 also displays the time series of PD_{peak} , OF, and TB_{cld} . As mentioned previously, to compute the latter two variables, all cloudy-sky scenes with TB below the " 3σ thresholds," shown as the dashed lines in Fig. 1, are used here. In addition, to remove some casual noise produced by only taking PD_{peak} values, PD from a relatively small TB window ($180K < TB_V < 210K$) is averaged (referred to as $\overline{PD_{peak}}$), showing that the major conclusions hold robustly against using 1 hr time interval, as well as against variations of the thresholds (e.g., using dash or dash-dot lines in Fig. 1 to compute OF and TB_{cld} or using slightly different windows to compute $\overline{PD_{peak}}$).

Similar to the findings from TRMM data, the diurnal cycle of $\overline{PD_{peak}}$ is the opposite of OF and total mass ($-TB_{cld}$), while the latter two go together tightly. However, the largest correlation coefficient is found when $\overline{PD_{peak}}$ leads the other two quantities by ~ 2 hours, when the correlation coefficient exceeds -0.9. That is to say, when $\overline{PD_{peak}}$ reaches its minimum (maximum) during the day, ice cloud coverage and total ice cloud mass reach their maximum (minimum) within ~ 2 hrs. This is the first study implying that ice crystal microphysics may play

a key role on the formation/dissipation processes of ice clouds. Furthermore, this leading time of 2 hrs is robust against using a time interval of 1 hr, but it would be “distorted” to 3 hrs if we use 3 hrs as the time interval for the analysis. Such a sensitivity exercise emphasizes the importance of having enough samples and small enough time steps in order to investigate the diurnal variation.

The only exception is between $\overline{PD_{peak}}$ and OF over ocean where the correlation is the largest without 5 hour advancement. This result changes with choosing different time interval so it's not a robust result. Since the diurnal cycle of $\overline{PD_{peak}}$ is too small over ocean to beat its own variability (error bars on Fig. 2a), the correlation among these three cloud parameters are not statistically significant over ocean anyway.

In summary, a strong diurnal cycle of GMI's 166 GHz PD is found for tropical ice clouds over land and a much weaker diurnal cycle over the ocean. The diurnal variations of PD lead those of the total ice cloud coverage and mass by ~ 2 hrs.

3. Interpretation and Radiative Transfer Model Simulations

As the observed PD is dominantly positive, by definition, ice particles in the ice cloud layer must possess anisotropic characteristics in terms of the bulk microphysical properties along the line of sight. In other words, the ice particles within this ice cloud layer must be aspherical microphysically and, more importantly, also aspherical on an integrated sense. Previous studies hence proposed that the majority of aspherical ice crystals should have oriented preferably along the horizontal direction rather than randomly oriented (Prigent et al., 2001, 2005; Davis et al., 2005, 2007; Zhou et al., 2012, 2013; Defer et al., 2014). GW17 took one step further that explained the entire bottom-up bell curve feature of the PD-TB relationship with a conceptual

model. In this model, when a cloud is optically thick, both V- and H-pol radiations are saturated at the same level, causing PD to diminish. By applying this hypothesis to a radiative transfer model (RTM), GW17 simulated the observed PD-TB relationship for 89, 166, and 640 GHz at the same time by controlling one parameter, called the “optical aspect ratio” (AR), defined as $AR \equiv \tau_V / \tau_H$. The ratio is not the typical “axial ratio” parameter often used to describe the eccentricity of an aspherical ice particle; it is the column integrated optical property difference between V-pol and H-pol at a given frequency, in the present case, 166 GHz. Further, by adjusting the value of AR, GW17 found the curvature of the PD-TB relationship changes, but the warm and cold ends remain converging to 0 (as expected theoretically) at roughly the same TB_V values. In other words, PD_{peak} is directly tied to the value of AR.

Following on the GW17 approach, the observed diurnal variation of the PD-TB relationship is simulated using different AR values in the same RTM as detailed in GW17. Briefly speaking about the setup, two parallel simulations are run at the same time; one with a regular extinction profile and the other profile is arbitrarily multiplied by a fixed AR value. Gamma distribution is employed for the particle size distribution, with the effective diameter fixed at 160 μm . By varying the cloud optical depth to create the dynamic range of TB, the difference between the two parallel runs creates the “PD-TB” bell curve observed (c.f., Section 4.2 of GW17). In this study, AR is changed from 1.0 to 2.0 with increments of 0.02 for each set of simulation. The “best-fit” AR value is then defined such that the standard deviation between the simulated PD and the observed counterpart reaches minimum (see Fig. 3a). In this way, the AR value is “retrieved” for different LSTs and its time series are displayed in Fig. 3b and 3c over the ocean and land surfaces, respectively. This AR “retrieval” is technically similar to a standard retrieval process except for not actually retrieving a physical quantity with a set of rigorous algorithms.

As expected, the variation of the “best-fit” AR is tightly correlated with the diurnal variation of $\overline{PD_{peak}}$. When the diurnal variation amplitude is small compared to the internal variability at a given LST, the “best-fit” AR is insensitive to the small change of $\overline{PD_{peak}}$. That’s the case over tropical ocean. On the other hand, when the tropical land convection and the associated anvil and cirrus clouds start to experience the most dramatic diurnal change from noon to late night, the “best-fit” AR value also changes accordingly.

The value of AR physically corresponds to an integrated result from a few ice microphysical parameters that impact τ_V/τ_H by definition. $\tau = \int_{z_{base}}^{z_{top}} \int_{D_{min}}^{D_{max}} N(D)A(D)dD dz$, where N is the number density, A is the cross section of the particle size perpendicular to the incoming radiation, D is the diameter, and z_{base} and z_{top} are the cloud base and top heights, respectively (Heymsfield et al., 2003). With V-pol and H-pol detecting radiation from the surface that penetrates up through the same ice cloud layer, only the aspherical particle shape and diameter at two specific directions that are perpendicular to V-pol and H-pol, assuming that the 100% horizontal-alignment is valid. Under this assumption, large (small) AR corresponds to high (low) axial ratio of the ice particles. That means over land, the majority of ice particles tend to become more and more sphere-like from morning (9 am) to afternoon (4 pm), and from then on horizontally oriented non-spherical ice crystals start to dominate the PD signal again.

This proposed diurnal variation of ice crystal orientation is consistent with the physics model of radiation-induced ice crystal growth (or the radiative effect on microphysics [(e.g., Zeng 2008)]). In the physics model, horizontally oriented ice crystals near the cloud top, in contrast to the vertically oriented ones, emit longwave radiation effectively to space, subsequently have low surface temperature, and thus can grow to precipitation-sized particles, which explains the positive value of the PD observed. Meanwhile, ice crystals near the cloud top absorb solar

radiation during daytime and consequently the radiation-induced crystal growth is modulated by solar radiation, which explains the diurnal variation of the PD shown in Figs. 1 and 2 (Zeng et al., 2016). The model also explains the delay of peak of ice cloud mass and coverage, since horizontally oriented ice crystals with larger PD (i.e., flatter) tend to quickly grow into precipitation-sized ones and fall out as precipitation, while ice crystals that are more sphere-like grow slower and stay as ice cloud for a longer time.

As for the relationship of AR to particle size, GW17 found its relationship to AR is quite complicated and nonlinear using a fully polarized RTM simulation (see Fig. 9 in GW17). GW17 found that the ice crystal with “column” shape overall matched the best with the observations, and the curvature of the PD-TB curve rises with the effective radius, But for certain other shapes, such as rosette with 7 branches, simulation results do not show the clear linear relationship between PD_{peak} and effective radius. Therefore, one cannot rush to the conclusion that the particle size growth exhibits a diurnal cycle. Other factors might also contribute to the diurnal variation of PD but are likely secondary (e.g., liquid cloud that can damp the PD and TB signals also exhibit its own diurnal cycle).

The 100% horizontal alignment is unlikely to occur in reality, and the mixing of different ice particle shapes may also vary diurnally. The better-mixed the shapes are (i.e., more percentage of random-orientation), the smaller the AR value is because AR is expected to vanish for the extreme situation of 100% random orientation. If the percentage of randomly oriented particles is the only or major contributor to the diurnal variation of PD_{peak} , then it indicates that along with the growth of deep convective systems from late morning to the early evening, ice particles also tend to become more and more randomly oriented. This makes sense as the vertical motion in deep convective cores tends to generate and maintain a more turbulent environment than that in

the ambient environment of the anvils and cirrus. However, this could not explain the ~ 2 hrs delay of the peak/trough of the diurnal cycles of ice cloud mass and coverage. Also, as indicated in the Appendix A, the PD_{peak} information indeed mostly comes from the differentiation of τ_V and τ_H for anvils, instead of from deep convective clouds as 166 GHz quickly saturates at the top several kilometers of the deep convective core. Therefore, the degree of turbulence, or randomness, inside the deep convective cloud is not a major contributor to the value of AR or PD_{peak} .

4. Conclusions

High-frequency passive microwave measurements, such as GMI 166 GHz channel, are sensitive to ice cloud scattering. Vertically and horizontally polarized microwave observations are found to differ in cloudy-sky because of the disparity of their optical thicknesses through an ice cloud layer with anisotropic bulk microphysical properties. As a result, the polarimetric radiance difference, or PD, can be used to infer cloud microphysical properties (i.e., ice crystal shape, size, and orientation).

The GPM precession orbit provides a valuable chance to study the diurnal variations of PD at 166 GHz in the tropics for the first time. The PD-TB relationship bears with a bottom-up bell curve that was investigated extensively in an earlier study of Gong and Wu [2017]. All bell curves can be represented by the peak PD amplitude, called PD_{peak} , which serves as a good measure to characterize the diurnal variation of the PD-TB curve. Similar to other macrophysical quantities like the area of coverage, occurring frequency, and total mass of ice clouds, PD_{peak} is found to vary by only 6% over tropical ocean, but vary dramatically ($\sim 38\%$) over tropical land.

The maximum and minimum of PD_{peak} occur at local morning and afternoon over tropical land, which lead the diurnal cycle of ice cloud mass and coverage by ~ 2 hrs with an opposite sign.

The observed diurnal variation of the PD-TB relationship can be explained quantitatively using a set of different AR values, because AR reflects a bulk effect of ice crystal shape and size in radiative transfer, and the diurnal variation in PD is linked directly to a variation in AR. Other microphysical properties, however, may also play a role in altering the PD-TB relationship as observed and need to be explored with more observations and accurate model representations of ice microphysical properties. Since radiation impacts ice crystal growth via crystal surface temperature (e.g., Zeng, 2008; Zeng et al., 2016), it can subsequently change AR, which in turn changes PD. Although we cannot fully understand the delay and anticorrelation of cloud mass and coverage with respect to PD, the delayed occurrence of ice cloud macro-physical properties indicates the importance of ice microphysics in formation/decay of ice clouds. It is imperative to include these processes in models to replicate the realistic cloud diurnal cycle and its radiative and hydrological effects.

This study exemplifies the power of passive microwave polarimetry in remotely sensing ice cloud microphysical properties. The 166 GHz is the highest frequency of polarized channels in GMI. Because ice cloud scattering is more significant at high frequencies, careful fusion of observations from multi-frequency polarized microwave/IR channels makes it feasible to infer both bulk ice particle size and shape simultaneously and allows global studies of ice cloud microphysics on diurnal, seasonal, and interannual time scales. Although it has been well known that ice microphysics are strongly tied together with the evolution of ice cloud macro-properties, this work identifies that understanding the variations in ice microphysics are necessary to predict, infer, and model the bulk properties of the ice clouds and their broader evolution (e.g.,

precipitation process). This study is a good exercise to manifest that new satellite instrumentation (e.g., GMI) with novel observational techniques (e.g., paired high-frequency microwave channels) may offer a valuable means to observe and understand the entire cloud-precipitation processes.

Appendix A: Where does the PD_{peak} come from?

In Gong and Wu (2017), the bottom-up bell curves of the PD-TB relationship from 89, 166, and 640 GHz observations are explained by the different penetration depth of V-pol and H-pol measurements through an ice cloud layer consisting of horizontally oriented nonspherical ice crystals. In this appendix, we present additional evidence to support this explanation. More importantly, this exercise answers directly to the types of ice cloud, their vertical levels, and how they contribute to the largest PD signal (PD_{peak}).

Two years (2014–2015) of collocated CloudSat-GMI data are compiled together to composite the Contoured Frequency by Altitude Diagram (CFAD) in Fig. A1b for the clouds that satisfy the criteria such that $7\text{ K} < PD < 20\text{ K}$ and $160\text{ K} < TB_v < 220\text{ K}$ (enclosed by the red rectangle box in Fig. A1a). This dataset is produced by Dr. Joe Turk at the Jet Propulsion Lab and details about this dataset can be found in Turk [2017]. To generate robust statistics, we employed two years of data since collocated GPM-CloudSat scenes are sparse. For CloudSat, 0 dBZ roughly separates the thin ice clouds (anvils, cirrus) with low reflectivity from thick ice clouds (thick anvils, deep convective cores) with high reflectivity.

As shown in CFADs for V-pol and H-pol, the largest disparity comes from clouds with reflectivity below 0 dBZ and height above 10 km. These clouds are apparently thin anvils (that at least 166 GHz V-pol can partially penetrate through) and cirrus clouds. When the ice cloud

becomes thicker and lower, 166 GHz passive microwave observations quickly saturates, and although 166 GHz are still sensitive to these clouds (down to cloud height as low as 2 km and as strong as 25 dBZ), the PD of 166 GHz no longer shows the disparity.

One possible explanation of the curvature of the PD-TB relationship that is proposed in GW17 is that turbulence in deep convective cores likely forces the nonspherical ice crystals to be well mixed (i.e., randomly oriented), in which way the PD eventually vanishes when TB gets cold. This exercise demonstrates that although this mechanism is quite plausible, 166 GHz PD measurements cannot identify the turbulence condition in thick ice clouds and therefore cannot be used to verify such a hypothesized mechanism.

Data Access

GMI Level-1 calibrated radiance data and CloudSat-GPM collocation dataset can be acquired from the Precipitation Processing System's (PPS) FTP server at arthurhou.pps.eosdis.nasa.gov. The radiative transfer model is coded and modified by the authors for this specific study. Interested readers are encouraged to contact the lead author directly for a copy of the model. All data used to make the figures in this manuscript are included in the supplementary materials. A README file illustrates the file format, content, and variable meanings.

Funding Information

Drs. Gong, Zeng, and Li were supported by the NASA CloudSat/CALIPSO project under grant NNX16AM06G for this work. In addition, Drs. Gong and. Wu were also supported by the NASA grants NNH16ZDA001N-ACMAP and NNH16ZDA001N-IIP. Drs. Zeng and Li were in addition supported by the PMM project under grant NNX16AE24G and NNX16AE25G, respectively.

367

368 **Acknowledgement**

369 This work benefited from discussions with Drs. Stephen Joe Munchak at NASA Goddard. We
370 thank the two anonymous reviewers for their insightful comments and suggestions. Special
371 thanks are extended to Dr. James L. Cogan and Ms. Nancy J. Simini of Technical Publications at
372 the US Army Research Lab for reading and copy-editing the paper.

373

374 **References**

375 Boukabara, S. A., Garrett, K., Chen, W. C., Iturbide-Sanchez, F., Grassotti, C., Kongoli, C.,
376 Chen, R. Y., Liu, Q. H., Yan, B. H., Weng, F. Z., Ferraro, R., Kleespies, T. J., and Meng, H.
377 (2011), MiRS: An All-Weather 1DVAR Satellite Data Assimilation and Retrieval System. IEEE
378 Transactions on Geoscience and Remote Sensing, 49(9), 3249-3272.

379 Chung, E. S., Sohn, B. J., Schmetz, J., and Koenig, M. (2007), Diurnal variation of upper
380 tropospheric humidity and its relations to convective activities over tropical Africa, Atmos.
381 Chem. Phys., 7, 2489–2502, doi:10.5194/acp-7-2489-2007.

382 Dai, A. and Trenberth, K. E. (2004), The diurnal cycle and its depiction in the community
383 climate system model, J. Climate, 17, 930–951.

384 Davis, C. P., D. L. Wu, C. Emde, J. H. Jiang, R. E. Cofield, and R. S. Harwood (2005), Cirrus
385 induced polarization in 122 GHz aura Microwave Limb Sounder radiances, *Geophys. Res. Lett.*,
386 **32**, L14806, doi:10.1029/2005GL022681.

387 Davis, C. P., Evans, K. F., Buehler, S. A., Wu, D. L., and Pumphrey, H. C. (2007), 3-D polarised
388 simulations of space-borne passive mm/sub-mm midlatitude cirrus observations: a case study,
389 Atmos. Chem. Phys., 7, 4149–4158, doi:10.5194/acp-7-4149-2007.

390 Defer, E., V. S. Galligani, C. Prigent, and C. Jimenez (2014), First observations of polarized
391 scattering over ice clouds at close-to-millimeter wavelengths (157 GHz) with MADRAS on
392 board the Megha-Tropiques mission, J. Geophys. Res. Atmos., 119, 12,301–12,316,
393 doi:10.1002/2014JD022353.

394 Duncan, D. I., and C. D. Kummerow (2016), A 1DVAR retrieval applied to GMI: Algorithm
395 description, validation, and sensitivities, J. Geophys. Res. Atmos., 121, 7415–7429,
396 doi:10.1002/2016JD024808.

397 Eriksson, P., B. Rydberg, M. Johnston, D. P. Murtagh, H. Struthers, S. Ferrachat, and U.
398 Lohmann (2010), Diurnal variations of humidity and ice water content in the tropical upper

399 troposphere, *Atmos. Chem. Phys.*, 10, 11519-11533.

400 Fu, Q. and K.-N. Liou (1993), Parameterization of the radiative properties of cirrus clouds, *J.*
401 *Atmos. Sci.*, 50, 2008-2025.

402 Gong, J. and Wu, D. L. (2014), CloudSat-constrained cloud ice water path and cloud top height
403 retrievals from MHS 157 and 183.3 GHz radiances, *Atmos. Meas. Tech.*, 7, 1873–1890,
404 doi:10.5194/amt- 7-1873-2014.

405 Gong, J. and Wu, D. L. (2017), Microphysical properties of frozen particles inferred from Global
406 Precipitation Measurement (GPM) Microwave Imager (GMI) polarimetric measurements, *Atmos.*
407 *Chem. Phys.*, 17, 1–17, 2017, doi:10.5194/acp-17-1-2017.

408 GPM X-Cal Working Group (2015), NASA Global Precipitation Measurement Level 1C
409 Algorithms, Version 1.4, https://pps.gsfc.nasa.gov/Documents/L1C_ATBD.pdf.

410 Hartmann, D. L., H. H. Hendon, and R. A. Houze, Jr. (1984), Some implications of the
411 mesoscale circulations in tropical cloud clusters for large-scale dynamics and climate. *J. Atmos.*
412 *Sci.*, **41**, 113-121.

413
414 Hartmann, D. L., J. R. Holton and Q. Fu (2001), The heat balance of the tropical tropopause,
415 cirrus and stratospheric dehydration, *Geophys. Res. Lett.*, 28 (10), 1969-1972.

416 Hartmann, D. L., and Berry, S. E. (2017), The balanced radiative effect of tropical anvil clouds, *J.*
417 *Geophys. Res. Atmos.*, 122, 5003–5020, doi:[10.1002/2017JD026460](https://doi.org/10.1002/2017JD026460).

418 Heymsfield, A. J., S. Matrosov, B. Baum (2003), Ice water path – optical depth relationships for
419 cirrus and deep stratiform ice cloud layers, *J. Atmos. Sci.*, 42, 1369 – 1390.

420 Hioki, S., P. Yang, B. A. Baum, S. Platnick, K. G. Meyer, M. D. King, and J. Riedi (2016),
421 degree of ice particle surface roughness inferred from polarimetric observations, *Atmos. Chem.*
422 *Phys.*, 16, doi: 10.5194/acp-16-7545-2016

423 Homeyer, C. R. and Kumjian, M. R. (2015), Microphysical characteristics of overshooting
424 convection from polarimetric radar observations, *J. Atmos. Sci.*, 72, 870–891.

425 Hong, G., G. Heygster, C. A. M. Rodriguez (2006), Effect of cirrus clouds on the diurnal cycle
426 of tropical deep convective clouds, *J. Geophys. Res.*, 111, D06209, doi: 10.1029/2005JD006208.

427 Hong, Y., G. Liu, J.-L. F. Li (2016), Assessing the Radiative Effects of Global Ice Clouds Based
428 on CloudSat and CALIPSO Measurements, *J. Clim.*, doi: [http://dx.doi.org/10.1175/JCLI-D-15-](http://dx.doi.org/10.1175/JCLI-D-15-0799.1)
429 [0799.1](http://dx.doi.org/10.1175/JCLI-D-15-0799.1).

430
431 Hou, A. Y., R. K. Kakar, S. Neeck, A. A. Azarbarzin, C. D. Kummerow, M. Kojima, R. Oki, K.
432 Nakamura, and T. Iguchi (2014), The Global Precipitation Measurement Mission. *Bull. Amer.*
433 *Meteor. Soc.*, **95**, 701–722.

434

435 Jiang, J. H., H. Su, C. Zhai, T. J. Shen, T. Wu, J. Zhang, etc. (2014), Evaluating the diurnal cycle
436 of upper-tropospheric ice clouds in climate models using SMILES observations, *J. Atmos. Sci.*,
437 72, 1022–1044, doi: 10.1175/JAS-D-14-0124.1.
438

439 Kiehl, J. T., J. J. Hack, and B. P. Briegleb (1994), The simulated Earth radiation budget of the
440 National Center for Atmospheric Research Community Climate Model CCM2 and comparisons
441 with the Earth Radiation Budget Experiment (ERBE), *J. Geophys. Res.*, 99 (D10), 20,815–20,827.

442 Liou, K. N., Y. Takano, P. Yang, and Y. Gu (2002), Radiative transfer in cirrus clouds: Light
443 scattering and spectral information, in *Cirrus*, edited by D. Lynch et al., pp. 265–296, Oxford
444 Univ. Press, New York.

445 Liu, C. and Zipser, E. J. (2008), Diurnal cycles of precipitation, clouds, and lightning in the
446 tropics from 9 years of TRMM observations, *Geophys. Res. Lett.*, 35, L04 819,
447 doi:10.1029/2007GL032437.

448 Millan, L., W. Read, Y. Kasai, A. Lambert, N. Livesey, J. Mendrok, H. Sagawa, T. Sano, M.
449 Shiotani, and D. L. Wu (2013), SMILES ice cloud products, *J. Geophys. Res.*, 118, 6468–6477,
450 doi: 10.1002/jgrd.50322.

451 Prigent, C., J. R. Pardo, M. I. Mishchenko, and W. B. Rossow (2001), Microwave polarized
452 signatures generated within cloud systems: Special Sensor Microwave Imager (SSM/I)
453 observations interpreted with radiative transfer simulations, *J. Geophys. Res.*, 106(D22), 28243–
454 28258.

455 Prigent, C., E. Defer, J. R. Pardo, C. Pearl, W. B. Rossow, and J.-P. Pinty (2005), Relations of
456 polarized scattering signatures observed by the TRMM Microwave Instrument with electrical
457 processes in cloud systems, *Geophys. Res. Lett.*, 32, L04810, Skofronick-Jackson, G. M. and J. R.
458 Wang (2000), The Estimation of Hydrometeor Profiles from Wideband Microwave Observations.
459 *J. Appl. Meteor.*, **39**, 1645–1656.

460 Raymond, D. J. and X. Zeng (2000), Instability and large-scale circulations in a two-column
461 model of the tropical troposphere. *Quart. J. Roy. Meteor. Soc.*, **126**, 3117–3135.

462 Sato, T., H. Miura, M. Satoh, Y. N. Takayabu (2009), Diurnal cycle of precipitation in the
463 tropics simulated in a global cloud-resolving model, *J. Clim.*, doi: 10.1175/2009JCLI2890.1.

464 Skofronick-Jackson, G. and Coauthors (2015), Global Precipitation Measurement Cold Season
465 Precipitation Experiment (GCPEX): For Measurement’s Sake, Let It Snow. *Bull. Amer. Meteor.*
466 *Soc.*, **96**, 1719–1741.

467 Soden, B. J. (2000), The diurnal cycle of convection, clouds, and water vapor in the tropical
468 upper troposphere, *Geophys. Res. Lett.*, 27, 2173–2176.

469 Tang, G., R. L. Panetta, P. Yang, G. W. Kattawar, P.-W. Zhai (2017), Effect of ice crystal
470 surface roughness and air bubble inclusions on cirrus cloud radiative properties from remote
471 sensing perspective, *J. Quant. Spec. Rad. Trans.*, 195, 119–131, doi: 10.1016/j.jqsrt.2017.01.016.

472 Tian, B., Soden, B. J., and Wu, X. (2004), Diurnal cycle of convection, clouds, and water vapor
473 in the tropical upper troposphere: Satellite versus a general circulation model, *J. Geophys. Res.*,
474 109, D10101, doi:10.1029/2003JD004117.

475 Turk, J. (2017), CloudSat-GPM Coincidence Dataset, Version 2A,
 476 https://pps.gsfc.nasa.gov/Documents/CSATGPM_COIN_ATBD.pdf
 477 Waliser, D. E., Li, J.-L. F., Woods, C. P., Austin, R. T., Bacmeister, J., Chern, J., Genio, A. D.,
 478 Jiang, J. H., Kuang, Z., Meng, H., Minnis, P., Platnick, S., Rossow, W. B., Stephens, G. L., Sun-
 479 Mack, S., Tao, W.-K., Tompkins, A. M., Vane, D. G., Walker, C., and Wu, D. (2009), Cloud ice:
 480 a climate model challenge with signs and expectations of progress, J. Geophys. Res., 114,
 481 D00A21, doi:10.1029/2008JD010015.
 482 Yang, G.-Y., and J. Slingo (2001), The diurnal cycle in the tropics, Mon. Weather Rev., 129,
 483 784–801.
 484 Zeng, X. (2008), The influence of radiation on ice crystal spectrum in the upper troposphere.
 485 *Quart. J. Roy. Meteor. Soc.*, **134**, 609-620.
 486 Zeng, X., W.-K. Tao, M. Zhang, A. Y. Hou, S. Xie, S. Lang, X. Li, D. Starr, and X. Li (2009a),
 487 A contribution by ice nuclei to global warming. *Quart. J. Roy. Meteor. Soc.*, 135, 1614-1629.
 488 Zeng, X., W.-K. Tao, M. Zhang, A. Y. Hou, S. Xie, S. Lang, X. Li, D. Starr, X. Li, and J.
 489 Simpson, (2009b), An indirect effect of ice nuclei on atmospheric radiation. *J. Atmos. Sci.*, 66,
 490 41-61.
 491 Zeng, X., G. Skofronick-Jackson, L. Tian, A. E. Emory, W. S. Olson and R. A. Kroodsma (2016),
 492 Analysis of the GMI/CoSMIR microwave polarization data for ice crystal modeling. The 2016
 493 Precipitation Measurement Mission (PMM) meeting, Houston, Texas, Oct. 24-28, 2016.
 494 Zhou, C., Yang, P., Dessler, A. E., Hu, Y., & Baum, B. A. (2012), Study of horizontally oriented
 495 ice crystals with CALIPSO observations and comparison with Monte Carlo radiative transfer
 496 simulations. *Journal of Applied Meteorology and Climatology*, 51(7), 1426-1439.

497

498 **Figure Titles:**

499 **Figure 1:** PD-TB_v curves at different local solar times (colors) over tropical ocean (a) and land
 500 (b). A curve is a simple connection of the mean values at each TB bin of the 2D PDF integrated
 501 from year 2015 of GMI observations at 166 GHz between 30°S and 30°N. The black dash lines
 502 indicate the 3σ threshold for computing the cloud occurring frequency and mean TB, and dash-
 503 dot lines exhibit the threshold for describing the PD-TB relationship.

504 **Figure 2:** Top: time series of the mean PD value for clouds with TB in the range of [180, 210] K
 505 (black), mean cloud occurring frequency (OF; red), and mean TB (TB_{cl}; blue; axis value is
 506 upside-down to match the physical meaning of total column ice mass) for clouds below the 3σ
 507 threshold (red) at tropical ocean (a) and land (b) during 2015. Bottom: lag-correlation between

508 the time series of PD and OF (red) and PD and TB_{cld} (blue) over ocean (c) and land (d).

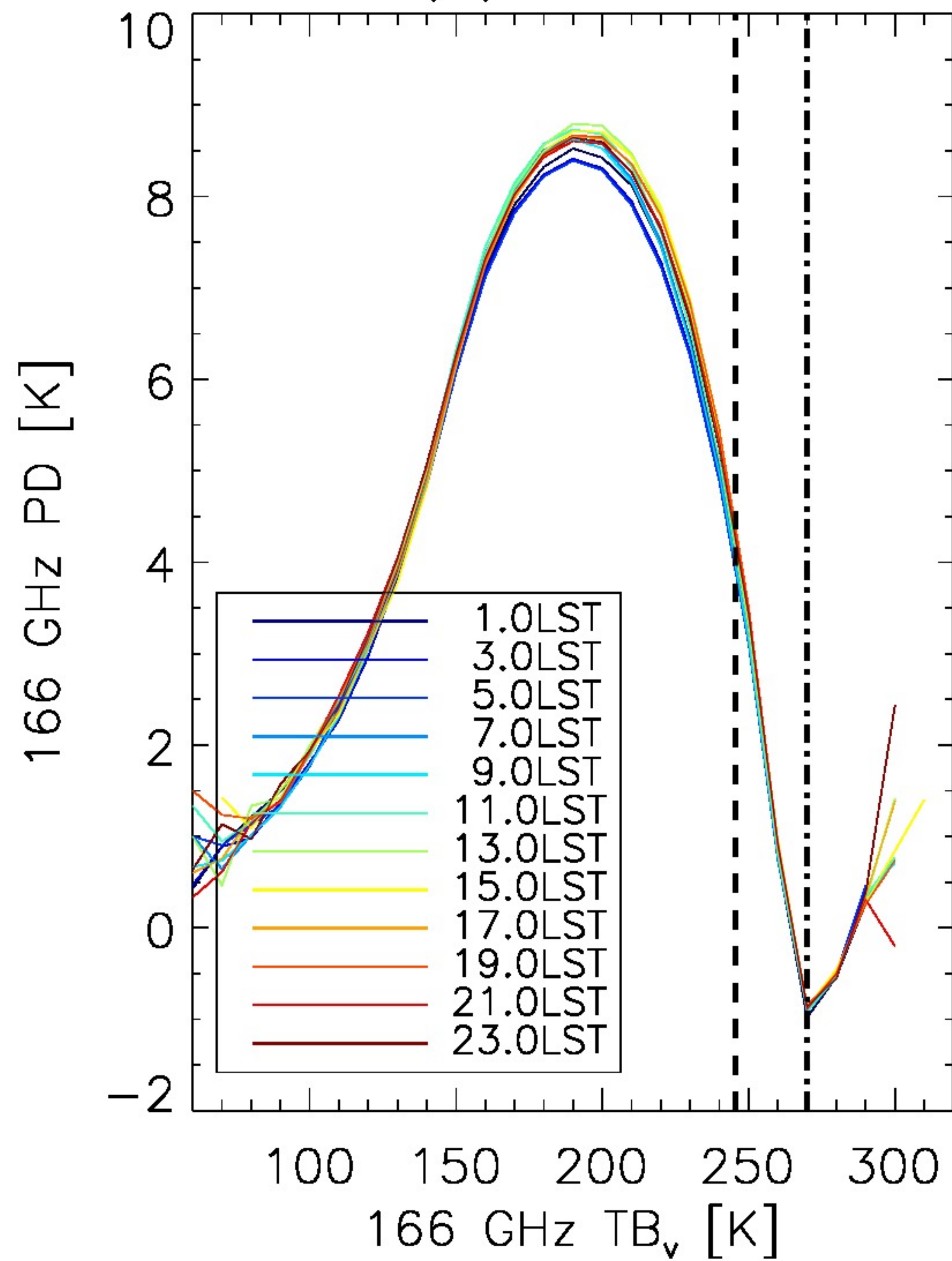
509 Positive/negative lag time corresponds to a lead/lag of the former time series to the latter ones.

510 **Figure 3:** (a) Example of how simulation compares with observations at 166 GHz. The simulated
511 166 GHz PD-TB_v relationships are shown in black lines with different AR values (AR varies
512 from thin to bold between 1.0 and 1.5 with an increment of 0.04); the top of the simulated results
513 shows the mean of the observed ensemble for the entire year of 2015 between the equator and
514 10°N with the variability shown in pink envelope (adapted from Fig. 8b of Gong and Wu, 2017).
515 The best-fit AR values derived from (a) for each time frame are plotted as stars in (b) and (c) for
516 ocean and land situations, respectively. Observations are taken from the curves shown in Fig. 1
517 and color legend is the same as Fig. 1. See the context for the definition of “best-fit”.

518 **Figure A1:** (a) Two-dimensional Probability Density Function (PDF) of PD (i.e., ΔTB) and TB_v
519 derived from GMI 166 GHz oceanic measurements during July 2015 collected between the
520 equator and 10°N. This figure is adapted from Fig. 3c of Gong and Wu (2017); (b) CFADs of
521 clouds selected from the red rectangle box enclosed area in (a). The black and red contours
522 correspond to 166 GHz V-pol and H-pol CFAD, respectively.

Figure 1.

(a) Ocean



(b) Land

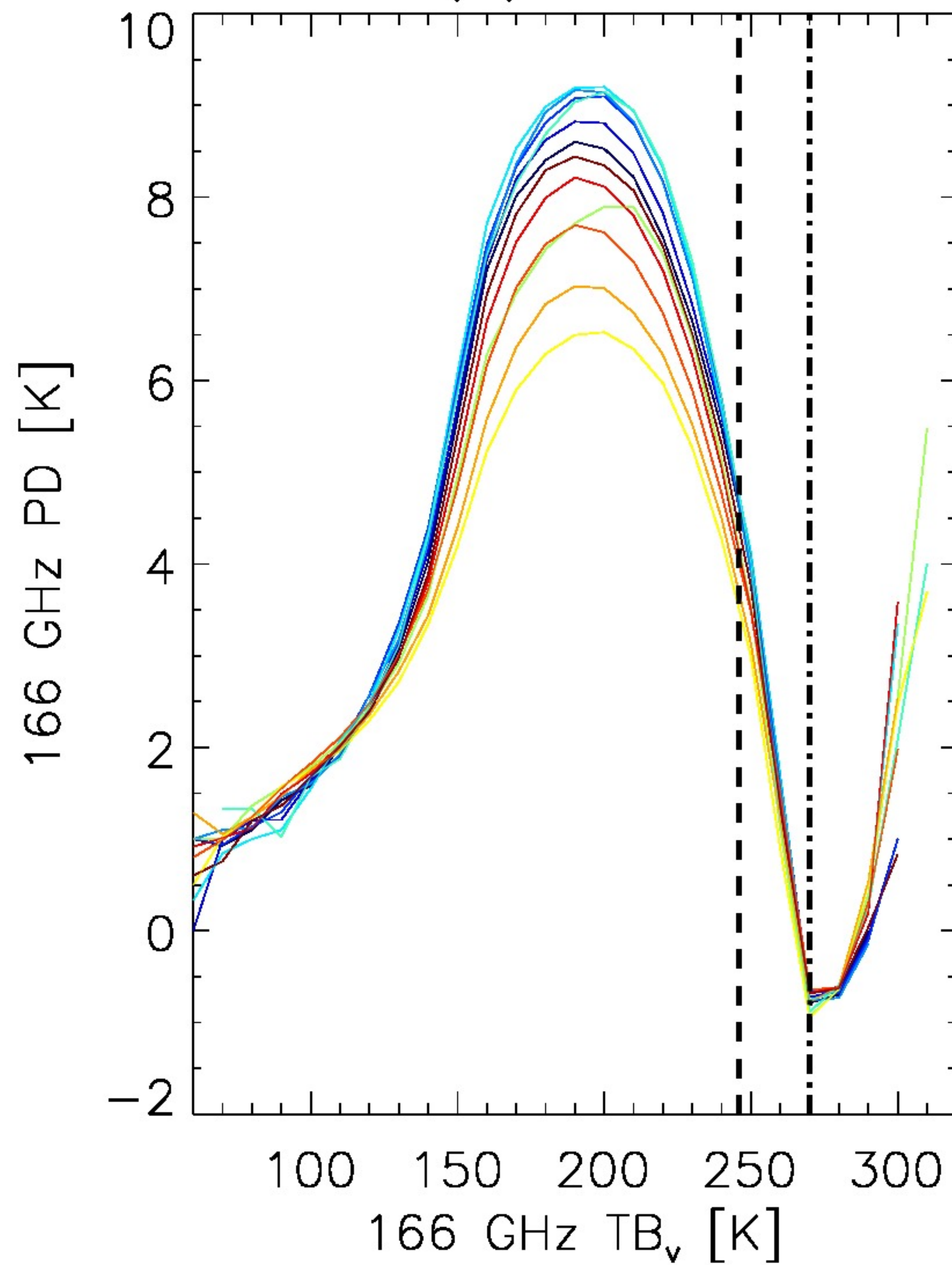
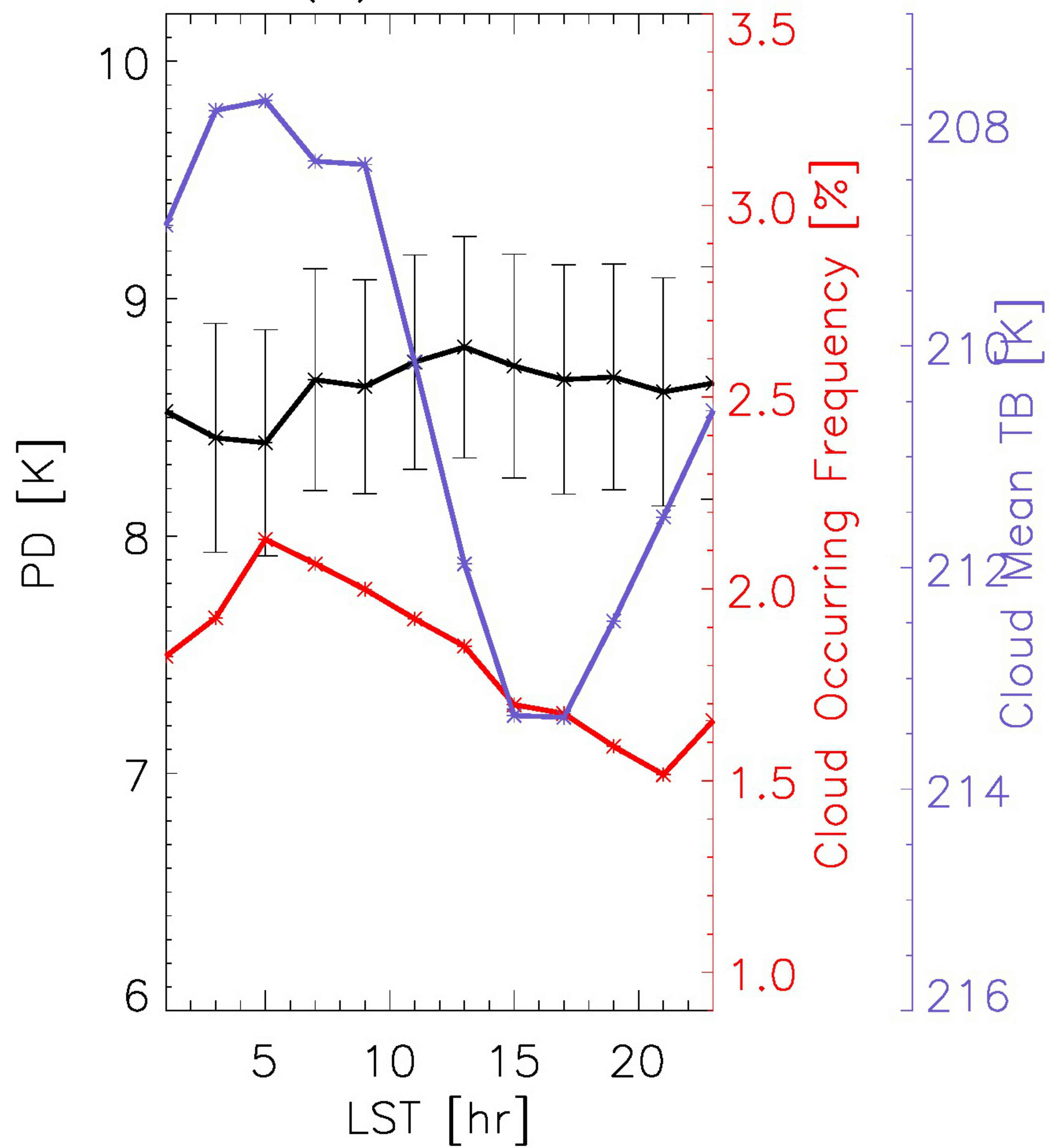
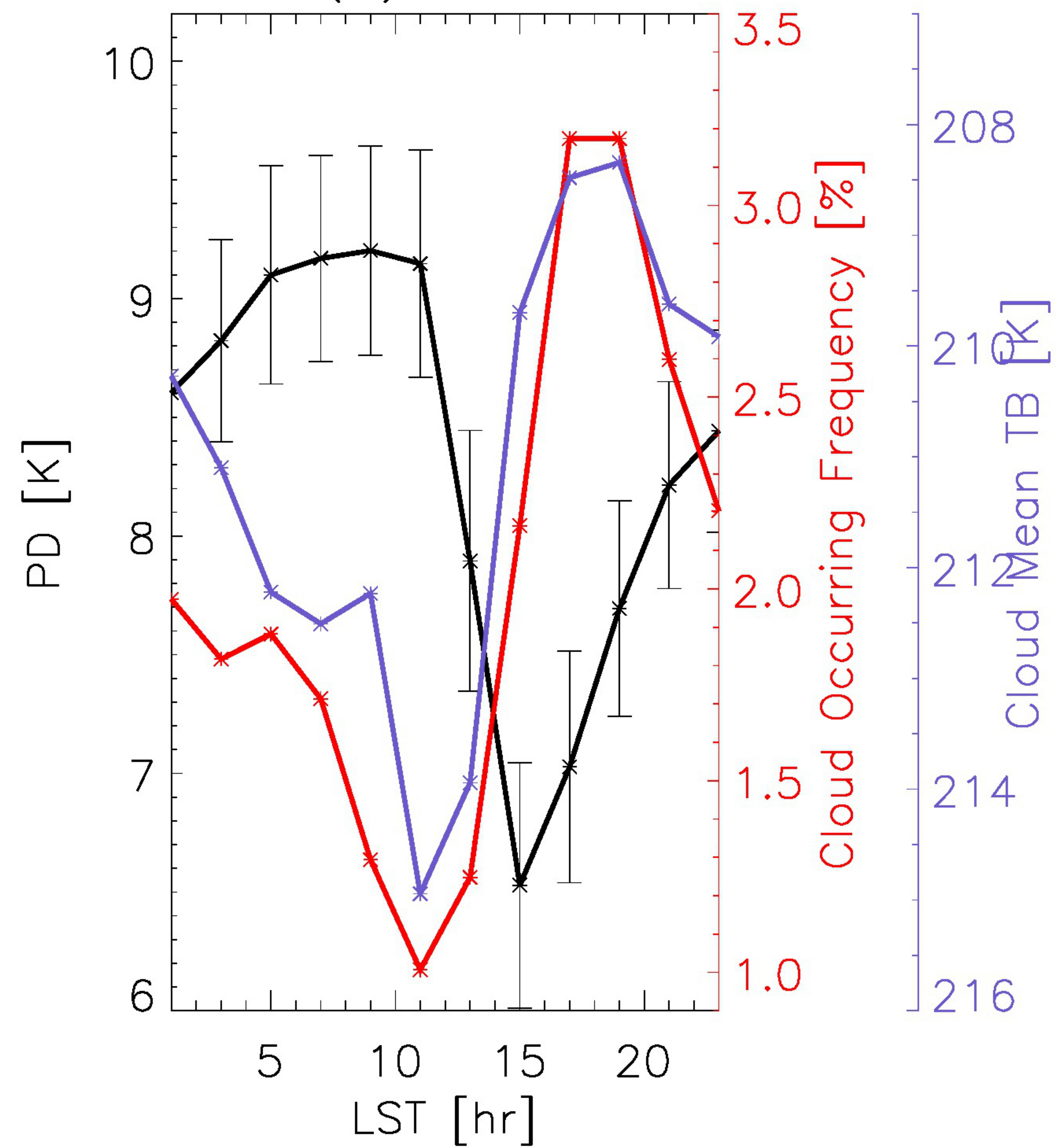


Figure 2.

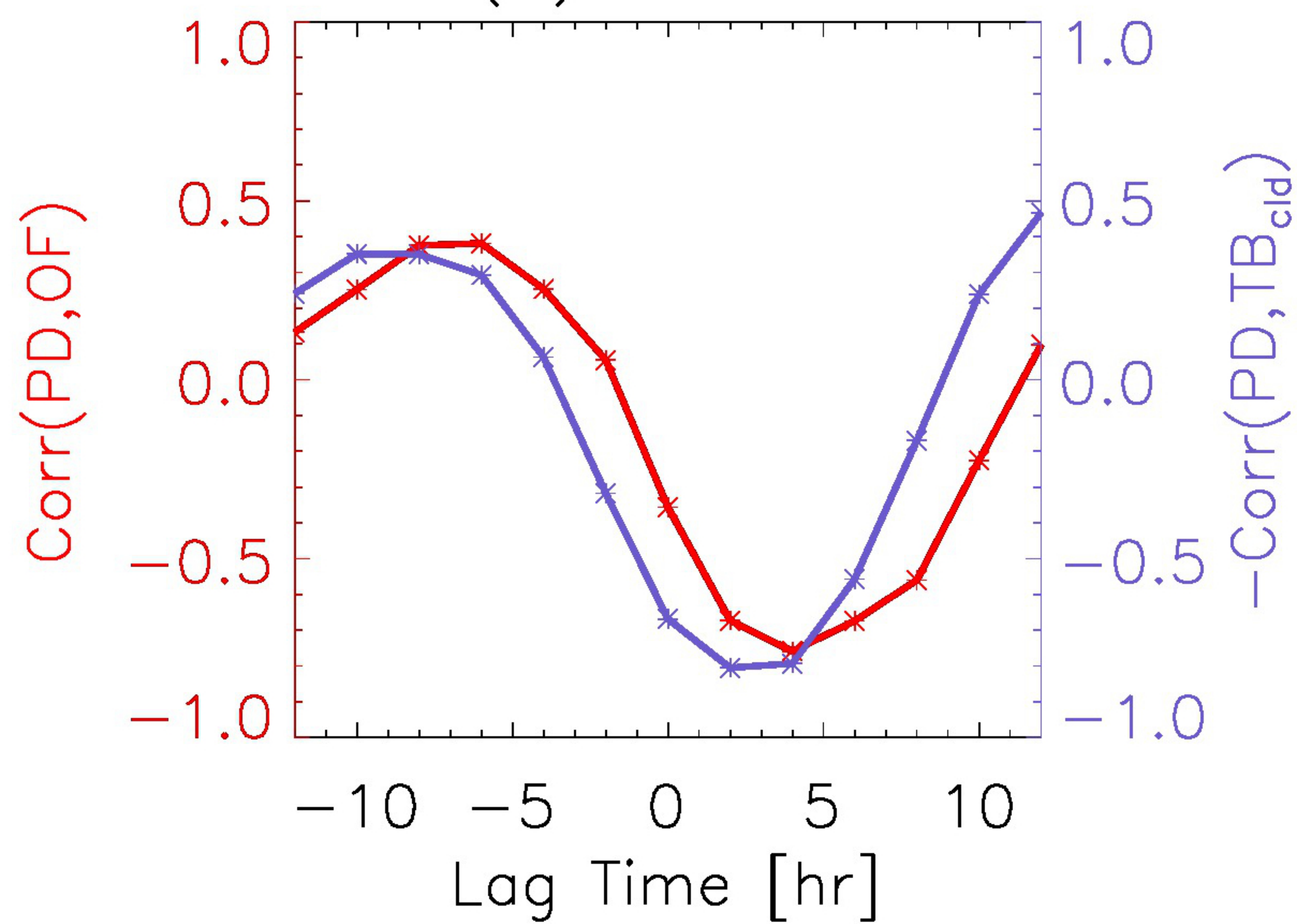
(a) Ocean



(b) Land



(c) Ocean



(d) Land

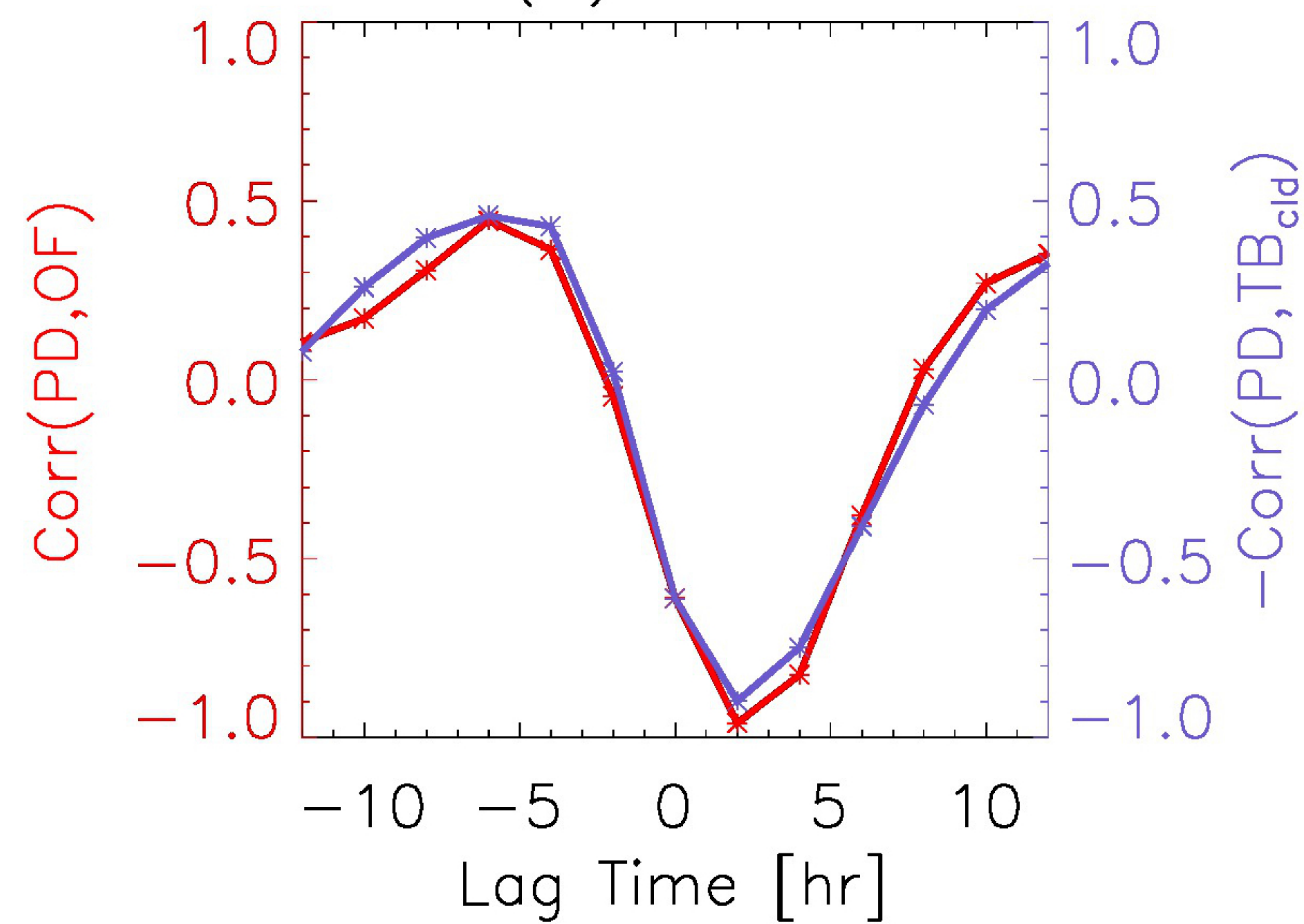


Figure 3.

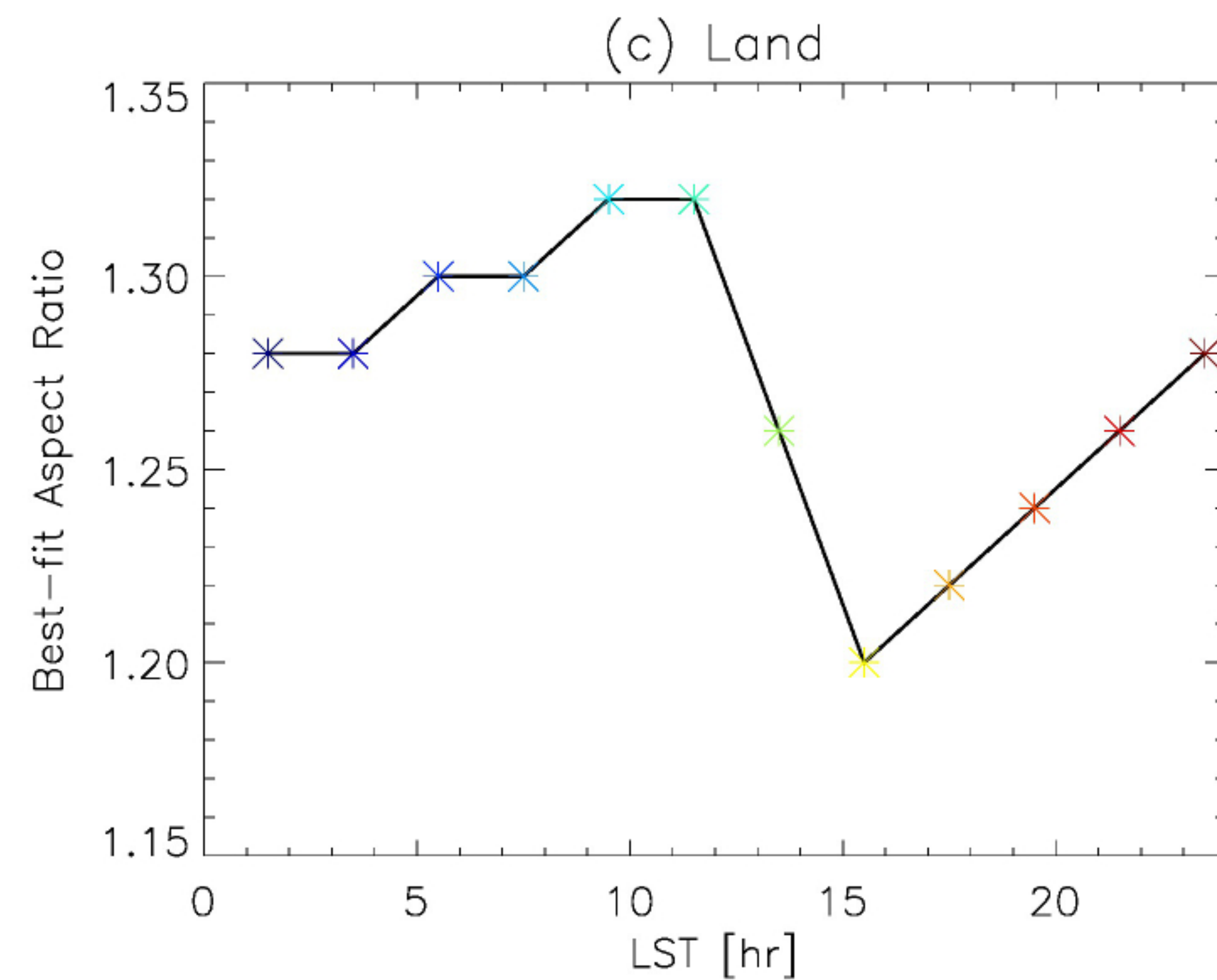
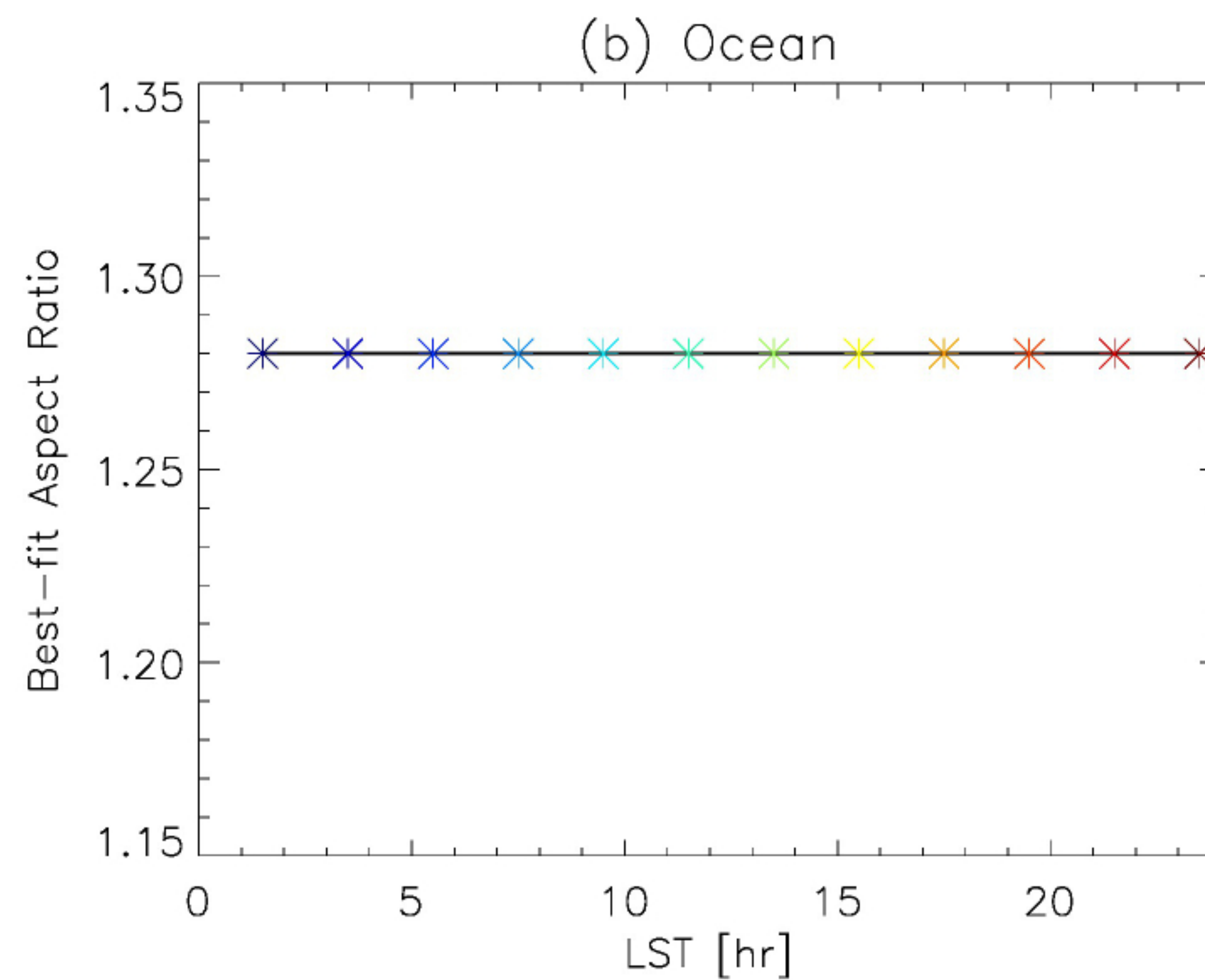
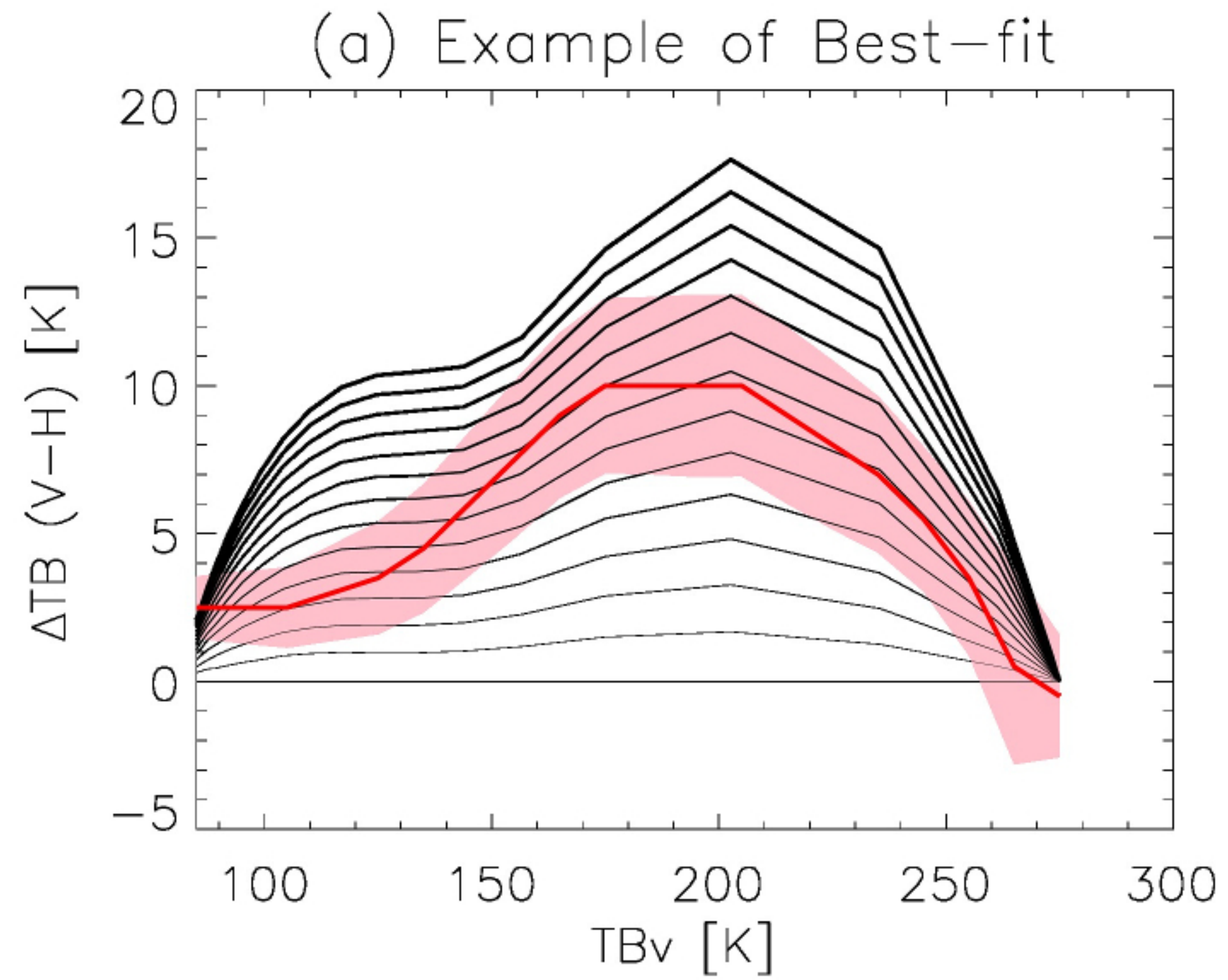
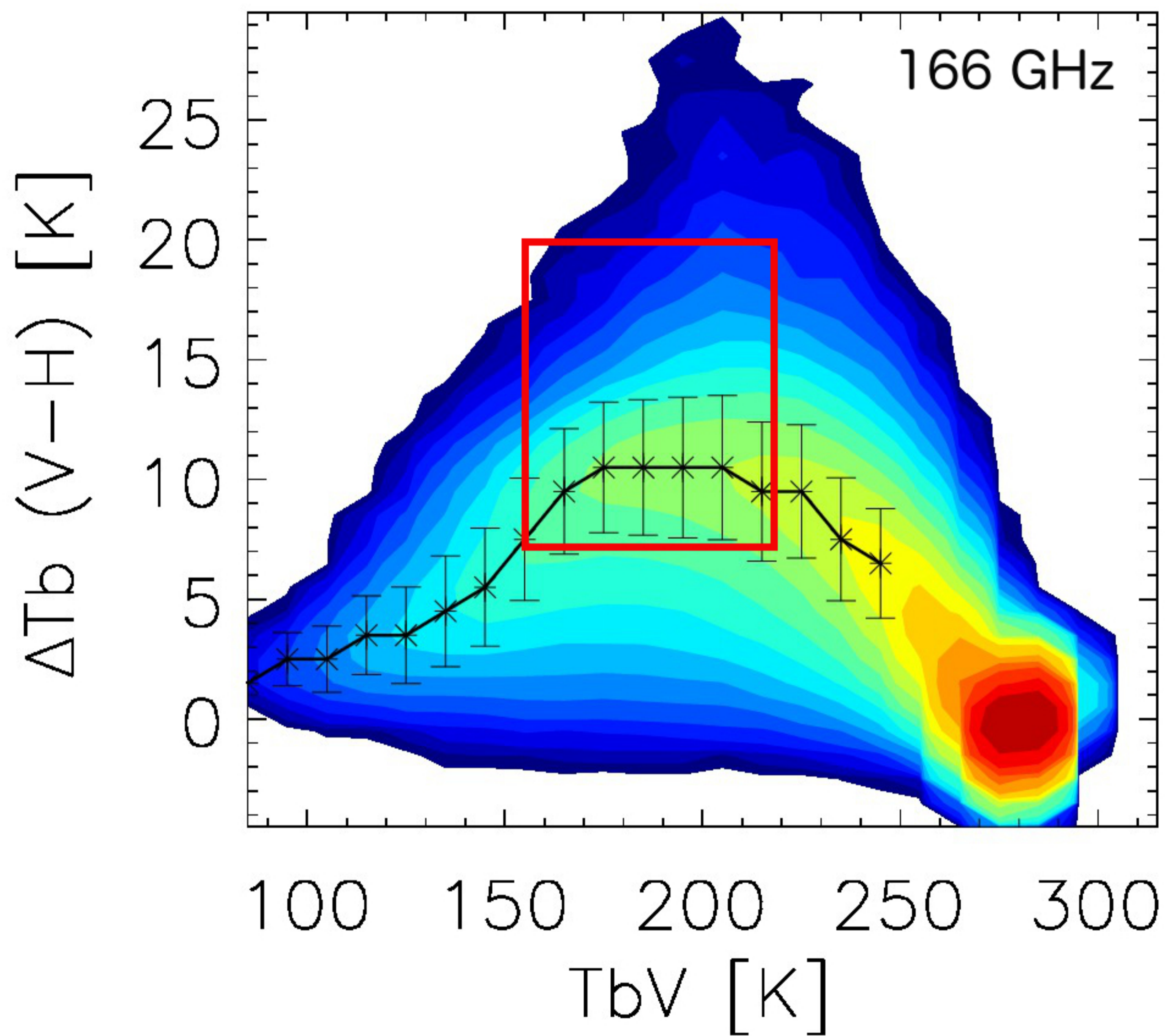


Figure A1.

(a) PDF, Ocean, [0, 10N], July 2015



(b) CFAD, [30S, 30N], 2014-2015

